Plasma Physics and Controlled
Fusion

PAPER

Quasi-monoenergetic multi-GeV electron acceleration by optimizing the spatial and spectral phases of PW laser pulses

IOP Publishing

Plasma Physics and Controlled Fusion

Plasma Phys. Control. Fusion **60** (2018) 064007 (10pp)

https://doi.org/10.1088/1361-6587/aabd10

Quasi-monoenergetic multi-GeV electron acceleration by optimizing the spatial and spectral phases of PW laser pulses

Junghun Shin[1], Hyung Taek Kim[1,2,7], V B Pathak[1], Calin Hojbota[1,6], Seong Ku Lee[1,2], Jae Hee Sung[1,2], Hwang Woon Lee[1], Jin Woo Yoon[1,2], Cheonha Jeon[1], Kazuhisa Nakajima[1], F Sylla[4], A Lifschitz[3], E Guillaume[3], C Thaury[3], V Malka[3,5] and Chang Hee Nam[1,6]

[1] Center for Relativistic Laser Science, Institute for Basic Science (IBS), Gwangju 500-712, Republic of Korea

[2] Advanced Photonics Research Institute, GIST, Gwangju 500-712, Republic of Korea

[3] Laboratoire d'Optique Appliquée (LOA), ENSTA ParisTech, CNRS UMR7639, École Polytechnique, Université Paris-Saclay, 828 Boulevard des Maréchaux, F-91762 Palaiseau, France

[4] SourceLAB SAS, 86 rue de Paris, F-91400 Orsay, France

[5] Weizmann Institute for Science, PO Box 26 Rehovot, 76100, Israel

[6] Department of Physics and Photon Science, GIST, Gwangju 500-712, Republic of Korea

E-mail: htkim@gist.ac.kr

Received 23 November 2017, revised 8 March 2018
Accepted for publication 10 April 2018
Published 30 April 2018

Abstract

Generation of high-quality electron beams from laser wakefield acceleration requires optimization of initial experimental parameters. We present here the dependence of accelerated electron beams on the temporal profile of a driving PW laser, the density, and length of an interacting medium. We have optimized the initial parameters to obtain 2.8 GeV quasi-monoenergetic electrons which can be applied further to the development of compact electron accelerators and radiations sources.

Keywords: laser, acceleration, LWFA, electron, wavefront, spectral phase

(Some figures may appear in colour only in the online journal)

1. Introduction

Laser wakefield acceleration [1] (LWFA) has been gaining its research interests due to its potential for compact electron accelerators and radiations sources [2–4] for innovative research in material and nuclear science. One of the main advantages in LWFA is the extremely high acceleration gradient, which is more than 1000 times greater than that of conventional radio-frequency accelerators. Since the LWFA uses laser-plasma interaction in a relativistic regime, all the physical processes, including initial plasma generation, the formation of plasma waves, electron bunch injection and acceleration of electrons, are highly nonlinear. This implies that the quality of accelerated electron beam using LWFA depends strongly on the initial experimental conditions of both driving laser pulse and plasma medium, such as intensity profile, wavefront and spectral phase of the laser pulse and the density and length of the interacting plasma.

The initial plasma conditions are important parameters for the laser propagation and acceleration processes. One of the fundamental parameters of a plasma medium is plasma frequency given by $\omega_p = \sqrt{4\pi n_e e^2/m}$, where n_e is electron density, and e and m are charge and mass of an electron. The plasma frequency is a crucial parameter in LWFA determining dephasing length ($L_{\rm dp} = 4\omega_0^2 c\sqrt{a_0}/3\omega_p^3$ in the nonlinear regime where ω_0 is the angular frequency of the laser, a_0 the normalized vector potential) and pump depletion distance ($L_{\rm pd} = (\omega_0/\omega_p)^2 c\tau$) [4]. Since they are inversely proportional to plasma frequency, reducing the plasma frequency lengthens the dephasing length and the pump depletion distance.

[7] Author to whom any correspondence should be addressed.

The fundamental plasma theory implies that low plasma density is advantageous for obtaining higher accelerated energy [4], while the electron bunch injection and self-guiding can be disturbed by the low plasma density. Consequently, the length and the density of a plasma medium should be controlled precisely to maximize the accelerated electron energy.

The characteristics of a driving laser are equally important as those of plasma parameters [5, 6]. The peak intensity of the laser pulse is determined by the focal volume, which is a product of focal spot area and pulse duration, and the energy concentration within the focus. The spatial and the spectral phases of laser pulse are the most important parameters for focal volume and energy concentration. Therefore, the spatial and spectral phases of the driving laser pulse can be varied to optimize the LWFA process. The control of the spatial phase of the driving laser pulse for the optimization of electron acceleration by LWFA has been studied using $\sim$1 terawatt, 0.5 kHz laser system [7]. The transverse intensity profile of the driving laser at its focus was manipulated by controlling the spatial phase of the laser pulse using a deformable mirror (DM) system with an iterative loop. This method is proved to be effective for improving the divergence of an electron beam, while its effect on controlling electron energy was restricted (see figure 4(b) in [7]) as the acceleration gradient of plasma wave strongly depends on the temporal profile of the laser pulse. On the other hand, an experiment on the control of spectral phases of driving petawatt (PW) laser pulse for LWFA experiment was recently demonstrated, in which the peak energy and the stability of accelerated electron beam were enhanced [8].

In this article, we present the interplay between the above-mentioned key parameters to generate quasi-monoenergetic multi-GeV electron beams using PW laser pulses. The spatial phase of a laser pulse was tuned so that the laser beam could be focused close to the diffraction limit, maximizing peak intensity of the laser pulse. The temporal phase, on the other hand, was controlled to have a slow-rising and fast-falling profile. The plasma density and length were adjusted for the optimal condition, which resulted in a low dark current, quasi-monoenergetic electron beam with its peak energy of 2.8 GeV.

2. Experiment method

A schematic of LWFA experiment using PW Ti:sapphire laser [9] at Center for Relativistic Laser Science (CoReLS), Institute for Basic Science (IBS) is shown in figure 1. A 25 J, 30 fs laser pulse with a central wavelength of 800 nm has a 10^{-8} contrast ratio level of amplified spontaneous emission starting 100 ps before the main pulse. A spherical mirror with a focal length of 6 m was used to focus the driving pulse. The length of the interacting gas cell (SourceLab, SL-ALC-HI [10]) can be varied from 0 to 20 mm in a vacuum, and the density of the gas can be adjusted by changing the backing pressure. A backing pressure of 130 mbar can be applied to maintain a uniform He gas density of 0.7×10^{18} atoms cm^{-3} for 10 mm gas cell, along the laser propagation axis with

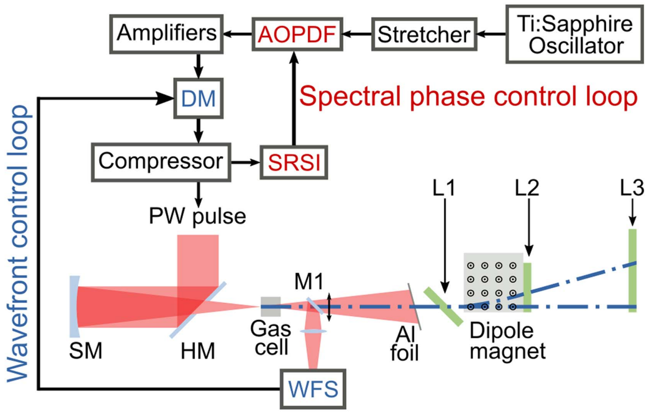

Figure 1. Schematic diagram of the wavefront-corrected, waveform-controlled LWFA experiment. It contains two feedback loops for the adjustments of wavefront and waveform of laser pulses. AOPDF: acousto-optic programmable dispersive filter, SRSI: self-referenced spectral interferometer, DM: deformable mirror, WFS: wavefront sensor, HM: holed-mirror, SM: spherical mirror for focusing PW pulse on the gas cell. L1, L2, and L3: scintillating (Lanex) screens at various locations.

2 mm density tails at the entrance and the exit of the gas cell. The driving laser pulse after the laser-plasma interaction is scattered off by a multi-layer aluminum foil. An electron spectrometer (ESM) to measure the energy of electron contains a dipole magnet with a uniform magnetic field of 1.33 T over 30 cm and three scintillating (Kodak Lanex) screens. First Lanex screen (L1) is imaged with a 12-bit visible charge-coupled device (CCD) to capture the electron beam profile. Second and third Lanex screens (L2 and L3) are imaged with intensified CCDs to record energy spectra. The distance between L2 and L3 screens was 0.53 m. This multi-screen configuration of ESM is suitable for an absolute energy calibration in laser-plasma experiments with a pointing instability problem [11].

In addition to this typical LWFA setup, the beamline has two feedback loops. One of the feedback loops controls the wavefront (spatial phase) of the driving laser pulse while the other loop controls the waveform (spectral phase). The wavefront control loop consists of a DM and a wavefront sensor to minimize the wavefront aberration of the laser pulse [12]. The spectral phase control loop consists of two acousto-optic programmable dispersive filters (AOPDFs) [13] and a self-referenced spectral interferometer (SRSI) [14] for temporal modulation of the laser pulse [15].

To deliver the maximum energy of the laser pulse for LWFA process, the wavefront of a driving laser pulse should be as flat as possible to reach diffraction-limited focus spot at the target plane. It is well known that Strehl ratio above 0.8 is required for diffraction-limited focus spot [16], which indicates that the root-mean-square error (RMSE) of wavefront should be below 0.075 λ (or 0.06 μm) for an 800 nm laser pulse according to Mahajan's equation [17]. The focus spot was optimized to a full width at half maximum (FWHM) diameter of 30 μm using the wavefront correction loop consisting of a wavefront sensor (SID4, [18]) at the end of

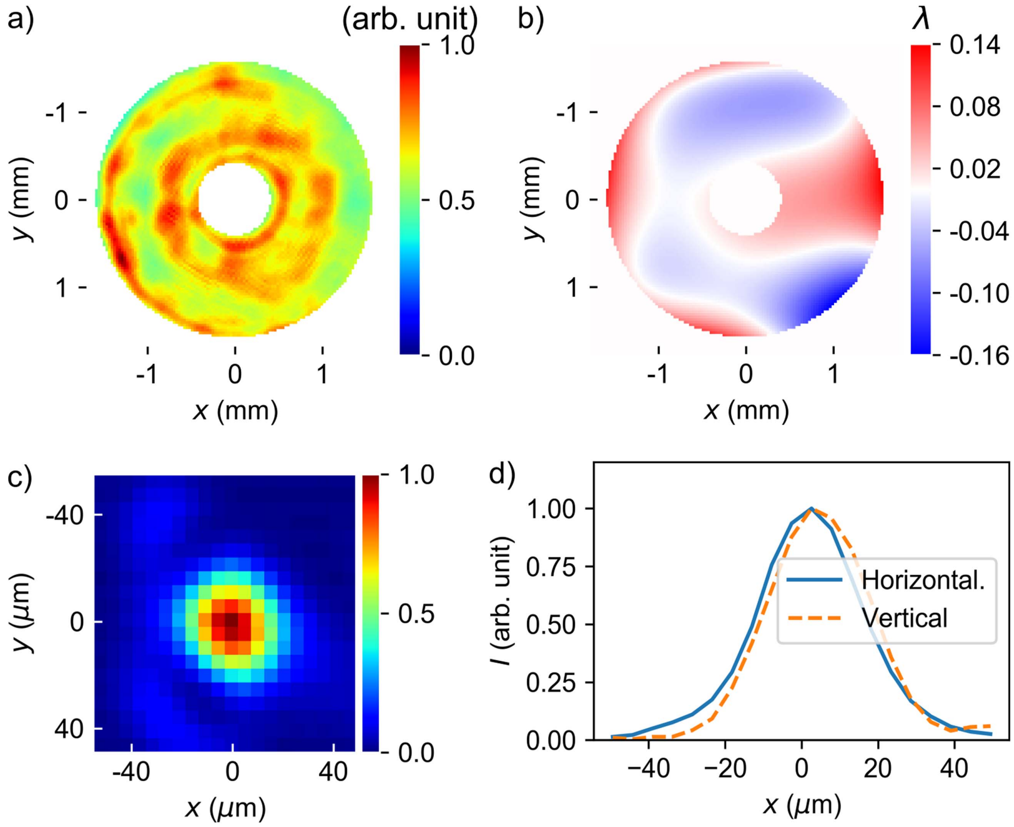

Figure 2. Beam profile of petawatt laser pulse after the wavefront correction using an iterative adaptive optics system consisting of a DM and a wavefront sensor. (a) and (b) show the intensity and the phase of the laser beam measured by the wavefront sensor. The beam profile of the optimized focus spot is shown in (c) with its line profiles shown in (d).

beamline and a bimorph DM [19] with 32 channels and 70 mm clear aperture placed between a boost amplifier and an achromatic beam expander before the PW compressor [12]. The DM is composed of three layers where the first layer is a glass with a broadband high reflection coating, the second layer is a large piezoplate that deforms the general curvature of the mirror to reduce the defocus of the beam, and the third layer is another piezoplate divided into 31 sections to compensate for various aberrations.

Figure 2 shows the typical intensity and phase profiles of the PW laser after wavefront correction. The intensity distribution after normalization had an average of 0.28 and an RMSE of 0.33. The phase distribution had a peak-to-valley phase difference of 0.3 λ and an RMSE of 0.03 λ, supporting the Strehl ratio well over 0.8 according to the Mahajan's equation [17]. Note, however, that actual focal spot can be worse than that expected from the Strehl ratio, possibly due to some misalignment of the imaging line to the wavefront sensor. The actual focal spot, measured with a 10-bit CMOS camera placed directly at the focal plane, is shown in figure 2(c) with its horizontal and vertical line profiles shown in figure 2(d). The FWHM beam diameter at the focus was 31.8 μm horizontally and 32.7 μm vertically with an f-number of the focusing optics of 30. Energy concentration in the first ring of the focal spot was 53%, while the Airy disk has 83.8% of energy in the same region. Without a proper wavefront correction, the electron acceleration by LWFA was extremely unstable, giving difficulties in studying the effects of variations in the waveform of a laser pulse on LWFA.

To control the waveform, i.e., electric field profile of a laser pulse, spectral phase terms were individually modified [20]. The spectral phase, $\varphi(\omega)$, of a laser pulse with a central frequency ω_0 can be represented in a Taylor series. Its second-order term, $\partial^2\varphi(\omega_0)/\partial\omega^2$, called group delay dispersion (GDD), determines linear chirp within the pulse without breaking the symmetry of the pulse envelope. Pulses with positive (or negative) GDD have linearly increasing (or decreasing) frequency component over time. The third-order term, $\partial^3\varphi(\omega_0)/\partial\omega^3$, called third-order dispersion (TOD), or quadratic chirp, produces an asymmetric temporal profile. We note that TOD can be achieved by mechanically detuning the grating angle of the PW laser compressor [21–24]. In this method, however, the effect of different spectral phase terms on LWFA is difficult to distinguish. In our experiments, one unit of SRSI is installed after the compressor in the PW beam line to precisely measure the spectral phase. The measured spectral phase is then fed back to AOPDF, installed after the pulse stretcher, to control individual terms of the spectral phase. Initially, a flat spectral phase was prepared using this iterative loop, and, then, individual spectral phase terms were adjusted to systematically study the waveform dependency of accelerated electron energy and its optimization.

3. Results and discussions

The LWFA process sensitively depends on the initial experimental conditions of the driving laser pulse and plasma medium. In following subsections, the effect of spectral chirps and plasma media on the LWFA process is investigated. In addition, we describe the details of optimization procedure for the LWFA experiments as well as an exemplary result of the optimization.

3.1. Effect of spectral chirp

Spectral phase of a laser pulse can affect the dynamics of LWFA as the ponderomotive force acting on electrons depends on the wavelength and the gradient of the laser intensity. In the experiments, we adjusted the GDD and TOD of the laser pulse independently using the spectral phase control, while the energy of the laser was unchanged. To figure out the role of spectral phases, PIC simulations are performed where qualitatively similar trends are observed.

In the experiments, before systematically investigating the dependence of the accelerated electron spectra on the spectral phase of a driving laser pulse, the spectral phases were initialized to zero using the spectral phase control loop. The wavefront aberrations were corrected as well to achieve the optimized focal spot shown in figure 2(c) using the adaptive optics system. The details of the experimental conditions and setup are reported in [8]. The change of electron spectrum and peak electron energy, depending on GDD of the driving laser pulse with a fixed plasma medium length of 10 mm is shown in figures 3(a) and (b), respectively. The figures show typical electron spectra and peak energies for different GDD of driving laser pulses. Electron beams generated with a chirp-free pulse have a broadband spectrum with a peak around 1 GeV, shown in figure 3(a). As the negative chirp was applied to the driving pulse, the peak electron energy decreased down to 600 MeV. On the other hand, when the positive chirp was applied, the peak energy increased to 1.6 GeV, and the optimized GDD value for the peak electron came out to be around 500 fs^2. Thus, the electron energy could be enhanced by manipulating the GDD of the laser pulse.

A surface plot describing the dependence of the peak electron energy on twenty combinations of GDDs and TODs is shown in figure 4. For each condition, the result of five shots was averaged. A general trend of an increase in electron energy was obtained with laser pulses that have positively chirped (positive GDD) and slowly rising (negative TOD) waveforms. On the contrary, laser pulses that have negatively chirped (negative GDD) and fast-rising (positive TOD) waveforms produced the lowest energy electron beams. It shows that the spectral phase is a critical laser parameter in the LWFA process where GDD seemed to have a greater influence on the peak electron energy than the TOD. In addition, the existence of the localized maximum in the surface map of electron energy as a function of GDD and TOD indicates that adaptive feedback control of LWFA with a high-repetition-rate PW laser would be feasible by tuning the waveform.

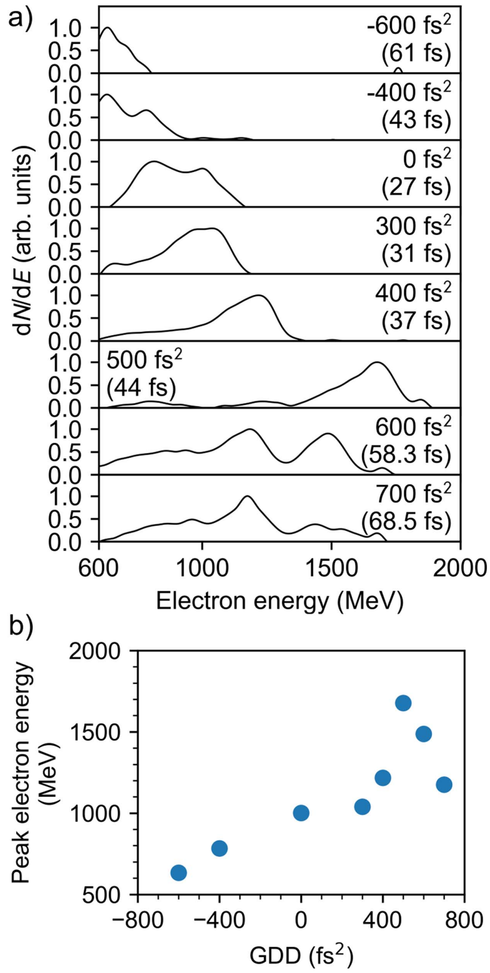

Figure 3. (a) Measured electron spectra obtained by controlling GDD and (b) peak electron energy with respect to GDD. For the electron density of 1.4×10^{18} electrons cm^{-3}, theoretical dephasing lengths were 14.4 mm for a chirped 44 fs pulse and 16.3 mm for the unchirped 27 fs pulse.

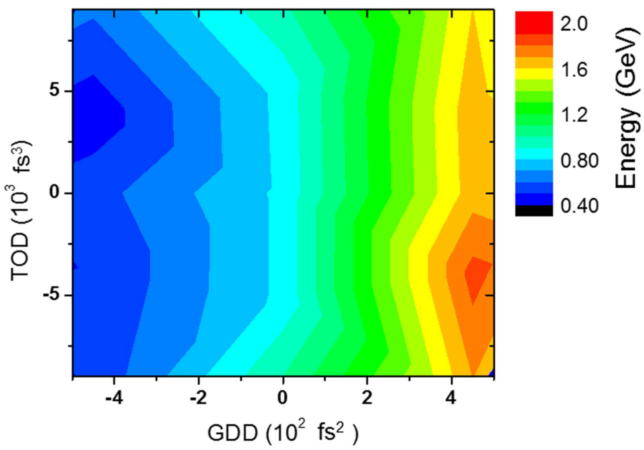

Figure 4. Map of the peak energy of accelerated electrons with respect to GDD and TOD of the driving chirped laser pulses.

The effect of spectral phase can be attributed to different dynamics of LWFA induced by the ponderomotive force exerted on electrons, which is proportional to the square of the laser wavelength and the gradient of the laser intensity. Positively chirped laser pulses have a stronger ponderomotive force at its leading edge, compared to negatively chirped laser pulses. To figure out the role of linear frequency chirp (GDD) in LWFA process, we performed a set of 2D PIC simulations using OSIRIS [25].

A simulation box (x–z) of dimensions $35 \times 48(c/\omega_p)^2$, moving at the speed of light along the z-direction, is constructed and divided into 480×6700 cells with 4×4 particles per cell. The plasma density increases linearly from 0 to 1×10^{18} electrons cm^{-3} for the first 2 mm of the medium and is kept constant for the rest of the medium. A linearly polarized laser pulse with a peak normalized vector potential $a_0 = 6$, central frequency $\omega_0 = 40\omega_p$, pulse length $L_{\mathrm{FWHM}} = 3.4c/\omega_p$ ($\tau_0 = 60$ fs), and transverse spot size $W_0 = 5.6c/\omega_p$ (30 μm), is initialized in the simulation box with a linear chirp coefficient of $\pm 1.0\omega_p^2$ (± 314 fs^2). The transverse profile of the laser pulse closely resembles the experimental laser pulse with side-wings. The peak of the side-wing is located 45 μm away from the laser axis with a Gaussian transverse profile of 10 μm width. The normalized vector potential is 10% of the main peak a_0. The unchirped laser pulse has a normalized vector potential of 8.25, 30 fs pulse length and a transverse spot size of 30 μm. These 2D PIC simulations show the different LWFA process and laser propagation with respect to the laser chirp.

The electron energy spectra from the PIC simulations with positively chirped, unchirped, and negatively chirped pulses are shown in figures 5(a)–(c). Energy spectra at z = 11.6 mm are summarized in figure 5(d). For the positive chirp case, a mono-energetic electron bunch accelerated over 500 MeV in the first bubble is observed at z = 3.6 mm, while continuous electron energy spectrum below 500 MeV is observed for the negative chirp case. The electron energy for the positive chirp increases rapidly and reaches 1.8 GeV at z = 7.4 mm, while the electron energy for the negative chirp saturates to 1 GeV. As the laser propagates further, the electron energy for the positive chirp increases up to 2.5 GeV. In the positive chirp case, the most of electrons around 0.5–1 GeV at the end of the medium are originated from the second bubble. On the other hand, for the negatively chirped pulse, the electron energy only reaches to 1.5 GeV at the end of the medium. For the unchirped laser pulse, the peak energy reaches up to 2 GeV. Overall, the positively chirped pulse provides well-defined electron injection and higher acceleration gradient in the early stage of acceleration than the negatively chirped pulse.

The laser pulse evolution is investigated to see the influence of frequency chirp on the laser propagation and acceleration process. Figure 6 shows the laser field evolution for the positively chirped, unchirped and negatively chirped pulses. The negatively chirped pulse leads to a significantly modulated laser field that leads to a stronger defocusing and wakefield compression takes place around $t = 1042\ \omega_p^{-1}$ (18.5 ps). This results in the expulsion of trapped electrons and no acceleration of particles from 1000 ω_p^{-1} (17.7 ps) to 1500 ω_p^{-1} (26.6 ps). In addition, the etching of the positively chirped pulse is stronger than that of the negatively chirped pulse [26], which enhances the effect of the strong ponderomotive push by the positively chirped pulse as the laser pulse propagates through the plasma medium. Consequently, the positively chirped pulse generates a strong ponderomotive potential at the pulse front and generates suitable plasma bubble structure for electron acceleration. For the unchirped pulse, even though the peak intensity is higher, due to shorter pulse length and strong beam loading effects, the final electron energy is lower than the positively chirped pulse.

Note that the effect of TOD had been simulated for two extreme cases, positive GDD with negative TOD and negative GDD with positive TOD, with a quasi-3D CALDER-Circ. PIC code [27] using the actual spectral intensity profile, GDD, and TOD of the experiment (see figure 5 in [8]). The simulation results show that the positively chirped slowly rising pulse undergoes very smooth propagation to the end of the plasma medium and yield twice the peak electron energy compared to the negatively chirped fast-rising pulse that undergoes strong modulation during propagation.

3.2. Effect of plasma medium

The parameters of the interacting plasma medium, such as its length and density, are also important for the optimization of LWFA. These parameters were carefully adjusted by controlling the length of the gas cell and the backing pressure of helium. Figure 7 shows the dependence of electron energy on cell length with three different GDDs of laser pulses at two backing pressures with electron densities of 2.1×10^{18} and 1.5×10^{18} cm^{-3}. At the optimum GDD (450 fs^2), the electron energy rapidly increased up to the cell length of 10 mm for both backing pressures. However, the lower backing pressure of 140 mbar gave a better result with an acceleration gradient of about 2.5 GeV cm^{-1} compared to the high-density case shown in figure 7(a). As the plasma medium lengthens, the electron energy may decrease due to the dephasing. The effect of GDD was more evident for the low-density case as shown in figure 7(b).

3.3. Optimization of LWFA

For the enhancement of electron energy, the following optimization procedure can be prescribed: (1) optimize the wavefront of a driving laser pulse to obtain near diffraction-limited focus spot, (2) adjust plasma length and decrease electron density close to the injection threshold, and (3) scan the spectral phase for tuning the LWFA process by waveform control. By adopting this procedure in LWFA experiments, a quasi-monoenergetic 2.8 GeV electron beam was obtained. The spatial profile, energy spectrum, and divergence of the optimized electron beam are shown in figure 8. The waveform of the PW laser pulse was synthesized to have a slow-rising (-4000 fs^3 TOD) edge with a positive (500 fs^2 GDD) chirp. The resulting 50 fs, 30 J laser pulse was focused on a 20 mm gas cell filled with helium at a low backing pressure of

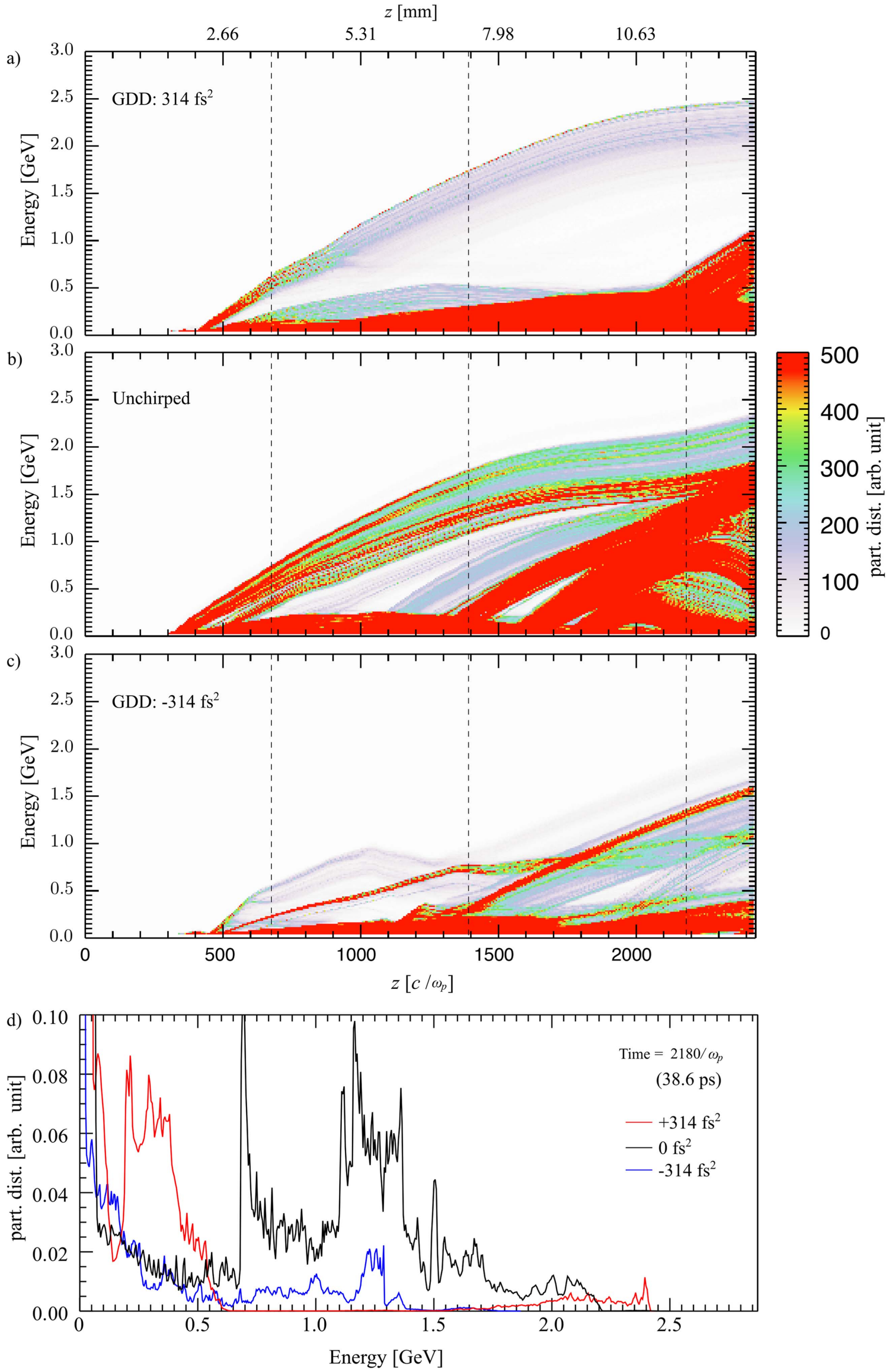

Figure 5. Electron energy spectra for (a) positively chirped pulse, (b) unchirped, and (c) negatively chirped pulses. The color code indicates the number of particles. Vertical dashed lines indicate where z, the propagation distance of the laser pulse, are 3.6, 7.4 and 11.6 mm. Electron spectra at $z = 11.6$ mm for the positively chirped (red line), unchirped (black line), and negatively chirped (blue line) pulses are shown in (d).

115 mbar, corresponding to the electron density of 1.2×10^{18} electrons cm^{-3}. The spatial profile recorded on Lanex phosphor screen L1 (figure 1) is shown in figure 8(a). From the spatial profile, electron beam divergence (FWHM) were found to be 1.91 mrad in the horizontal direction and 2.09 mrad in the vertical direction as shown in figure 8(b). Electron spectra recorded on Lanex phosphor screens L2 and L3 (figure 1) are shown in figures 6(c) and (d), respectively. The energy spread $\Delta E/E$ of the highest energy peak at 2.8 GeV is estimated to be 22% with a measurement resolution of 10%

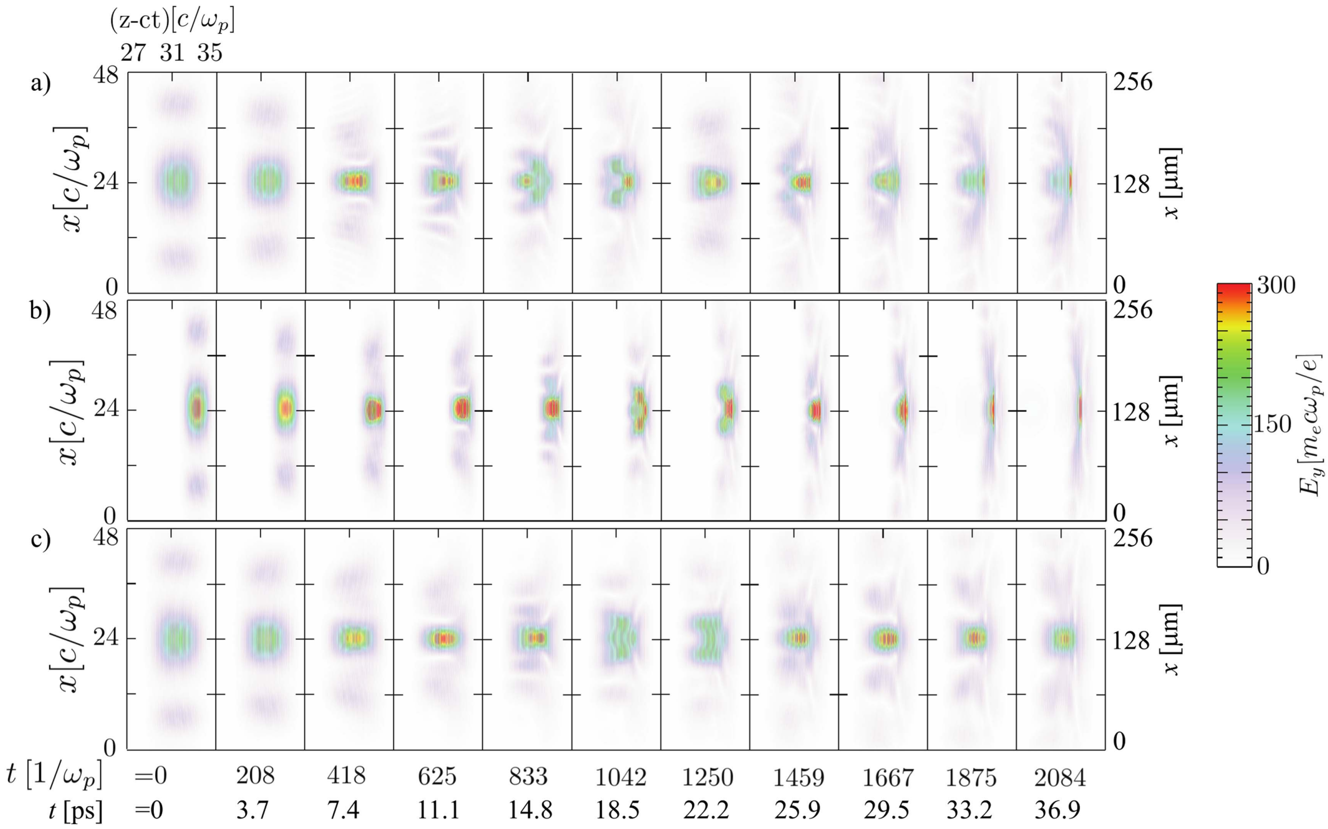

Figure 6. Laser evolution over time for (a) the negatively chirped, (b) unchirped, and (c) the positively chirped laser pulses.

with dark current suppressed up to 1.5 GeV. The charge of electrons with energy higher than 1.5 GeV was about 50 pC. We succeeded to increase electron energy by increasing plasma length (10–20 mm) and laser energy (25–30 J), and lowering electron density (2.1×10^{18}–1.2×10^{18} electrons cm^{-3}), compared to our previous experiment where we obtained 2 GeV electron beam [8]. The obtained peak energy of 2.8 GeV matches well with the energy gain of 2.74 GeV using the scaling law in [4].

The measured electron energy has an instrumental broadening effect from the ESM. Therefore, to accurately measure the electron energy distribution, a simple calculation is necessary. With an assumption of the electron energy spectrum being uniform over the entire spatial profile of the electron beam, the measured spectrum can be derived by convoluting the electron energy and spatial profile on the detection plane. Thus, the electron energy spectrum is deconvoluted to estimate the actual spectrum as it is shown in figure 8 with a red dashed line. This deconvolution is an iterative process where the ESM signal is approximated as a superposition of four Gaussian peaks. Each peak has parameters that determine its height, width, and central energy. The parameters of the Gaussian peaks are varied until a good match is reached as it is shown in figure 8(e). The green dotted line shows the convoluted spectrum with estimated electron spectrum and electron beam cross-section of figure 8(b). The convoluted spectrum matches well with the measured spectrum. The estimated energy spread with the deconvolution method came out to be around 9.6%. This shows that with the optimization of spatial and spectral phases of PW laser pulses, it is possible to produce quasi mono-energetic 2.8 GeV electron beam with a low dark current and energy spread below 10%.

For further electron energy enhancement, each step in the optimization procedure can be improved. For this study, the wavefront was corrected to be as flat as possible to generate diffraction-limited focus spot. As the first step, it might be possible to use deliberately manipulated wavefront to control electron acceleration process, as demonstrated for the electron profile optimization with a TW, kHz laser system [7]. Using iterative feedback from the electron beam profile and its power, a DM can be modulated to generate the optimum wavefront for the most efficient electron acceleration. However, this would require a PW laser with high-repetition-rate, e.g., $\geqslant$5 Hz, according to our experience with the closed loop focal spot optimization system. As the second step, the density of the interacting medium can be further improved. The decrease in electron density close to the injection threshold of $\sim 1 \times 10^{18}$ electrons cm^{-3} [28] may bring instability in self-injection and a fluctuation in electron energy. To enhance the electron energy further, the stabilization of electron injection should be addressed in the low electron density regime, which might be possible with ionization injection [29–33] or density gradient injection schemes [34–37]. For lower electron density, a higher laser power is necessary to enable injection and a longer plasma medium is needed for sufficient acceleration. The development of a stable high power PW laser and a new

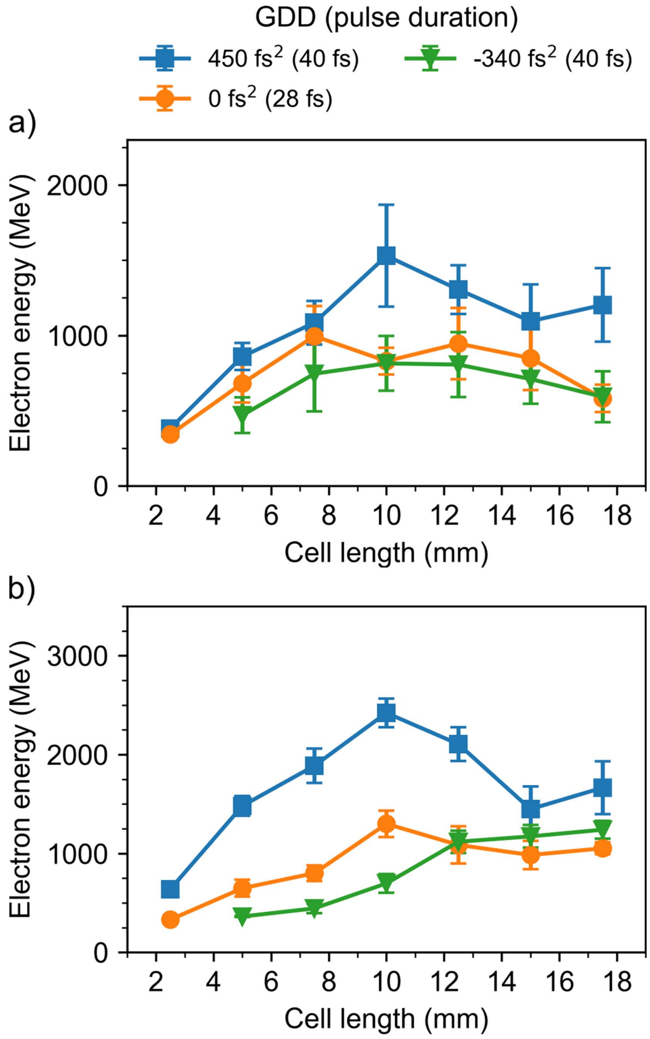

Figure 7. Dependence of peak electron energy on gas cell length with different GDD of the driving laser pulse and backing pressure. (a) He backing pressure of 200 mbar, corresponding to 2.1×10^{18} electrons cm^{-3}. Theoretical dephasing lengths were 8.0 mm for experiments with 40 fs laser pulses, and 8.8 mm for 28 fs laser pulses. (b) He backing pressure of 140 mbar, corresponding to 1.5×10^{18} electrons cm^{-3}. Theoretical dephasing lengths were 13.3 mm for experiments with 40 fs laser pulses and 14.5 mm for 28 fs laser pulses.

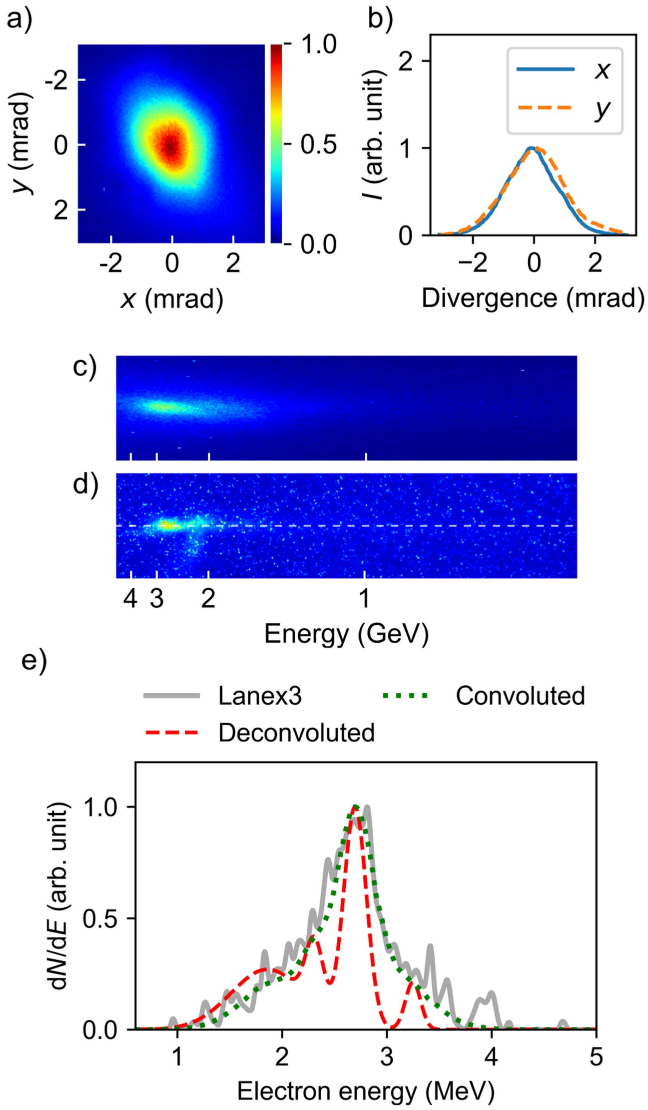

Figure 8. An example of a quasi-monoenergetic electron acceleration through the optimization procedure using a 20 mm gas cell filled with He gas. (a) First Lanex screen image (L1 in figure 1) for monitoring the electron beam profile. (b) Horizontal and vertical line profiles of (a). (c) Electron energy spectrum monitored on the second Lanex screen (L2 in figure 1) and (d) that on the third Lanex screen (L3 in figure 1). (e) Electron energy measured on (d) is shown in gray solid line. Deconvoluted spectrum is shown in red dashed line. Reconstructed spectrum (convolution of the deconvoluted spectrum) is shown in green dotted line.

gas cell supporting a longer plasma medium with an appropriately designed density profile would be the first step for reaching higher electron energy. Currently, the feedback is between the pulse duration measurement (SRSI) and the spectral phase modulator (AOPDF) for making a flat initial spectral phase. As there is a localized maximum condition in the map of electron energy plotted as a function of GDD and TOD (figure 4), as the third step, we may set a feedback loop consisting of ESM and AOPDF for maximizing the accelerated electron energy.

4. Conclusion

Quasi-monoenergetic multi-GeV electron acceleration was demonstrated by optimizing the spatial and spectral phases of driving PW laser pulses and plasma medium length and its density in LWFA experiments. After making the wavefront of the laser pulse as flat as possible and controlling the electron density to be close to the injection threshold, the LWFA process showed a strong dependence on spectral phase. Flat wavefront, near-injection threshold electron density, slow-rising and fast-falling waveform were found to be optimal for generating low dark current, quasi-monoenergetic electron beam peaked at 2.8 GeV. The demonstrated optimization technique and procedure might be improved further to have more precise control of electron beam divergence and electron energy. The above methods can be easily implemented in high intensity laser beamlines for compact multi-GeV electron accelerators, facilitating the development of ultra-short high-energy photon sources such as betatron radiation [38, 39], undulator x-ray [2], x-ray free-electron laser [40, 41] and Compton γ-ray [42, 43] sources.

Acknowledgments

Replacement: This work was supported by Institute for Basic Science (IBS-R012-D1), Korean Institute of Science and Technology Information (KSC-2016-C2-0046), and GIST through 'Research on Advanced Optical Science and Technology' grant in 2017. Authors would also like to acknowledge Jorge Vieira and Luis O Silva for their valuable suggestions and discussions.

ORCID iDs

Hyung Taek Kim https://orcid.org/0000-0002-6050-2374
V B Pathak https://orcid.org/0000-0003-4193-7556
Calin Hojbota https://orcid.org/0000-0002-4320-7584

References

[1] Tajima T and Dawson J M 1979 Laser electron accelerator *Phys. Rev. Lett.* **43** 267
[2] Fuchs M *et al* 2009 Laser-driven soft-x-ray undulator source *Nat. Phys.* **5** 826–9
[3] Esarey E, Schroeder C B and Leemans W P 2009 Physics of laser-driven plasma-based electron accelerators *Rev. Mod. Phys.* **81** 1229–85
[4] Lu W *et al* 2007 Generating multi-GeV electron bunches using single stage laser wakefield acceleration in a 3D nonlinear regime *Phys. Rev. Spec. Top.—Accel. Beams* **10** 061301
[5] Beaurepaire B *et al* 2015 Effect of the Laser Wave Front in a Laser-Plasma Accelerator *Phys. Rev.* X **5** 031012
[6] Ferri J *et al* 2016 Effect of experimental laser imperfections on laser wakefield acceleration and betatron source *Sci. Rep.* **6** 27846
[7] He Z-H, Hou B, Lebailly V, Nees J A, Krushelnick K and Thomas A G R 2015 Coherent control of plasma dynamics *Nat. Commun.* **6** 7156
[8] Kim H T *et al* 2017 Stable multi-GeV electron accelerator driven by waveform-controlled PW laser pulses *Sci. Rep.* **7** 10203
[9] Yu T J, Lee S K, Sung J H, Yoon J W, Jeong T M and Lee J 2012 Generation of high-contrast, 30 fs, 15 PW laser pulses from chirped-pulse amplification Ti:sapphire laser *Opt. Express* **20** 10807
[10] Brandi F, Giammanco F, Conti F, Sylla F, Lambert G and Gizzi L A 2016 Note: real-time monitoring via second-harmonic interferometry of a flow gas cell for laser wakefield acceleration *Rev. Sci. Instrum.* **87** 086103
[11] Cha H J *et al* 2012 Absolute energy calibration for relativistic electron beams with pointing instability from a laser-plasma accelerator *Rev. Sci. Instrum.* **83** 063301
[12] Jeong T M *et al* 2007 Wavefront correction and customization of focal spot of 100 TW Ti:sapphire laser system *Japan. J. Appl. Phys.* **46** 7724–30
[13] Tournois P 1997 Acousto-optic programmable dispersive filter for adaptive compensation of group delay time dispersion in laser systems *Opt. Commun.* **140** 245–9
[14] Oksenhendler T *et al* 2010 Self-referenced spectral interferometry *Appl. Phys.* B **99** 7–12
[15] Liu C *et al* 2014 Adaptive-feedback spectral-phase control for interactions with transform-limited ultrashort high-power laser pulses *Opt. Lett.* **39** 80
[16] Born M and Wolf E 1999 *Principles of Optics: Electromagnetic Theory of Propagation, Interference and Diffraction Of Light* (Cambridge: Cambridge University Press)
[17] Mahajan V N 1983 Strehl ratio for primary aberrations in terms of their aberration variance *J. Opt. Soc. Am.* **73** 860–1
[18] Bon P, Maucort G, Wattellier B and Monneret S 2009 Quadriwave lateral shearing interferometry for quantitative phase microscopy of living cells *Opt. Express* **17** 13080–94
[19] Kudryashov A, Alexandrov A, Zavalova V, Rukosuev A and Samarkin V 2007 Adaptive optics and high power pulse lasers *Proc. SPIE 6346, XVI Int. Symp. on Gas Flow, Chemical Lasers, and High-Power Lasers* p 634629
[20] Weiner A M 2009 *Ultrafast Optics* (Hoboken: Wiley)
[21] Leemans W P *et al* 2002 Electron-yield enhancement in a laser-wakefield accelerator driven by asymmetric laser pulses *Phys. Rev. Lett.* **89** 174802
[22] Schroeder C B *et al* 2003 Frequency chirp and pulse shape effects in self-modulated laser wakefield accelerators *Phys. Plasmas* **10** 2039–46
[23] Hafz N A M 2011 Utilizing asymmetric laser pulses for the generation of high-quality wakefield-accelerated electron beams *Nucl. Instrum. Methods Phys. Res.* A **654** 592–6
[24] Rao B S, Moorti A, Naik P A and Gupta P D 2013 Effect of chirp on self-modulation and laser wakefield electron acceleration in the regime of quasimonoenergetic electron beam generation *Phys. Rev. Spec. Top.—Accel. Beams* **16** 091301
[25] Fonseca R A *et al* 2002 OSIRIS: a three-dimensional, fully relativistic particle in cell code for modeling plasma based accelerators *ICCS 2002: Int. Conf. on Computational Science— Proc., Part III (Amsterdam, The Netherlands, 21–24 April 2002)* (Berlin: Springer) pp 342–51
[26] Pathak V B, Vieira J, Fonseca R A and Silva L O 2012 Effect of the frequency chirp on laser wakefield acceleration *New J. Phys.* **14** 023057
[27] Lifschitz A F, Davoine X, Lefebvre E, Faure J, Rechatin C and Malka V 2009 Particle-in-Cell modelling of laser–plasma interaction using Fourier decomposition *J. Comput. Phys.* **228** 1803–14
[28] Kim H T *et al* 2013 Enhancement of electron energy to the multi-GeV regime by a dual-stage laser-wakefield accelerator pumped by petawatt laser pulses *Phys. Rev. Lett.* **111** 165002
[29] McGuffey C *et al* 2010 Ionization induced trapping in a laser wakefield accelerator *Phys. Rev. Lett.* **104** 025004
[30] Pak A, Marsh K A, Martins S F, Lu W, Mori W B and Joshi C 2010 Injection and trapping of tunnel-ionized electrons into laser-produced wakes *Phys. Rev. Lett.* **104** 025003
[31] Liu J S *et al* 2011 All-optical cascaded laser wakefield accelerator using ionization-induced injection *Phys. Rev. Lett.* **107** 035001
[32] Pollock B B *et al* 2011 Demonstration of a narrow energy spread, $\sim$0.5 GeV electron beam from a two-stage laser wakefield accelerator *Phys. Rev. Lett.* **107** 045001
[33] Chen M, Esarey E, Schroeder C B, Geddes C G R and Leemans W P 2012 Theory of ionization-induced trapping in laser-plasma accelerators *Phys. Plasmas* **19** 033101

[34] Geddes C G R *et al* 2008 Plasma-density-gradient injection of low absolute-momentum-spread electron bunches *Phys. Rev. Lett.* **100** 215004
[35] Gonsalves A J *et al* 2011 Tunable laser plasma accelerator based on longitudinal density tailoring *Nat. Phys.* **7** 862–6
[36] Buck A *et al* 2013 Shock-front injector for high-quality laser-plasma acceleration *Phys. Rev. Lett.* **110** 185006
[37] Thaury C *et al* 2015 Shock assisted ionization injection in laser-plasma accelerators *Sci. Rep.* **5** 16310
[38] Esarey E, Shadwick B A, Catravas P and Leemans W P 2002 Synchrotron radiation from electron beams in plasma-focusing channels *Phys. Rev.* E **65** 056505
[39] Rousse A *et al* 2004 Production of a keV x-ray beam from synchrotron radiation in relativistic laser-plasma interaction *Phys. Rev. Lett.* **93** 135005
[40] Couprie M E *et al* 2016 An application of laser–plasma acceleration: towards a free-electron laser amplification *Plasma Phys. Control. Fusion* **58** 034020
[41] Nakajima K *et al* 2012 Laser-driven table-top x-ray FEL *Free Electron Lasers* ed S Varro (Rijeka: InTech)
[42] Ta Phuoc K *et al* 2012 All-optical Compton gamma-ray source *Nat. Photonics* **6** 308–11
[43] Powers N D *et al* 2013 Quasi-monoenergetic and tunable x-rays from a laser-driven Compton light source *Nat. Photonics* **8** 28–31